Corrosion Science 199 (2022) 110172

Contents lists available at ScienceDirect

Corrosion Science

journal homepage: www.elsevier.com/locate/corsci

Hydrogen uptake during active CO_2-H_2S corrosion of carbon steel wires in simulated annulus fluid

Ellen Synnøve Skilbred [a,*], Simona Palencsár [b], Arne Dugstad [b], Roy Johnsen [a]

[a] Department of Mechanical and Industrial Engineering, Norwegian University of Science and Technology, 7034 Trondheim, Norway
[b] Institute for Energy Technology, P.O. Box 40, NO-2027, Kjeller, Norway

ARTICLE INFO

Keywords:
Carbon steel A
Hydrogen permeation B
SEM B
XRD B
Hydrogen absorption C

ABSTRACT

The hydrogen uptake of five carbon steel wires exposed to a corrosive CO_2/H_2S environment where protective film formation was not favorable was measured. The hydrogen uptakes decreased with the accumulation of retained carbide for most of the materials. It is assumed that hydrogen adsorbed on carbides at some distance from ferrite will not easily diffuse to the steel, hence giving the beneficial effect. This effect was not observed for the material with the lowest carbon content. Apart from this material, the hydrogen uptake increased with the carbon content, probably due to hydrogen trapping on ferrite-cementite interfaces.

1. Introduction

Flexible pipes have been used for oil and gas transportation since the 1970′s. They consist of several polymeric and metallic layers, such as carcass, inner liner, pressure armor wires, tensile armor wires and outer sheath. The annular space where the tensile steel armor wires are located is normally dry at start up but chemical species like CO_2, H_2S and H_2O can diffuse from the bore through the polymer layers into the annulus and create a corrosive environment. If the outer sheath is damaged, seawater may also enter the annulus. The free volume in the annulus is low compared to the area of the steel armor wires which gives rapid accumulation of dissolved corrosion products and a higher pH level than normally seen for CO_2 corrosion of carbon steel pipelines [1]. The liquid in the flexible pipe annulus is expected to become highly supersaturated with dissolved corrosion products and that will promote the formation of protective $FeCO_3$ and FeS films under normal operation. Corrosion rates below 0.01 mm y^{-1} are usually measured under such conditions [1–3]. However, upset conditions like air or seawater ingress, continuous high water condensation (backflow from vent tubes) and partial inhibition can reduce the supersaturation and prevent or weaken the protective films.

During pure CO_2 corrosion, the most likely cathodic reactions are [4,5].

$$2H^+ + 2\ e^- \rightarrow H_2 \quad (1)$$

$$2H_2CO_3 + 2\ e^- \rightarrow H_2 + 2HCO_3^- \quad (2)$$

The H^+ can be formed by water dissociation, but the rate of hydrogen evolution is enhanced by the presence of CO_2 due to the two dissociation steps of the carbonic acid [6]. When the concentrations of Fe^{2+} and CO_3^{2-} ions exceed their solubility limits they can form iron carbonate films. The dominant anodic reaction is the dissolution of iron in water and the overall reaction for CO_2 corrosion in steels is [5,7].

$$Fe + CO_2 + H_2O \rightarrow H_2 + FeCO_3 \quad (3)$$

$FeCO_3$ with good adhesion and coverage of the steel surface can retard the diffusion of species to and from the steel surface [8]. The adhesion of the $FeCO_3$ film is dependent on the presence of iron carbides, and the carbide size and distribution become important since the corrosion products are better adhering to the carbides than to the ferrite matrix [9].

Small amounts of H_2S can also diffuse into the annulus and give a mixed CO_2 and H_2S corrosion mechanism. The general equation for precipitation of ferrous sulfide can be written as [7].

$$Fe^{2+} + H_2S \rightarrow FeS + H_2 \quad (4)$$

The formation of hydrogen gas requires adsorption of H^+ on the metal or carbide surface. While adsorbed, H^+ is reduced to elemental H and may absorb into the metal and cause hydrogen embrittlement (HE). Hydrogen embrittlement is a failure mechanism that relies on the presence of elemental hydrogen and mechanical stress in a susceptible

* Corresponding author.
E-mail address: ellen.s.skilbred@ntnu.no (E.S. Skilbred).

https://doi.org/10.1016/j.corsci.2022.110172
Received 8 November 2021; Received in revised form 19 January 2022; Accepted 10 February 2022
Available online 12 February 2022

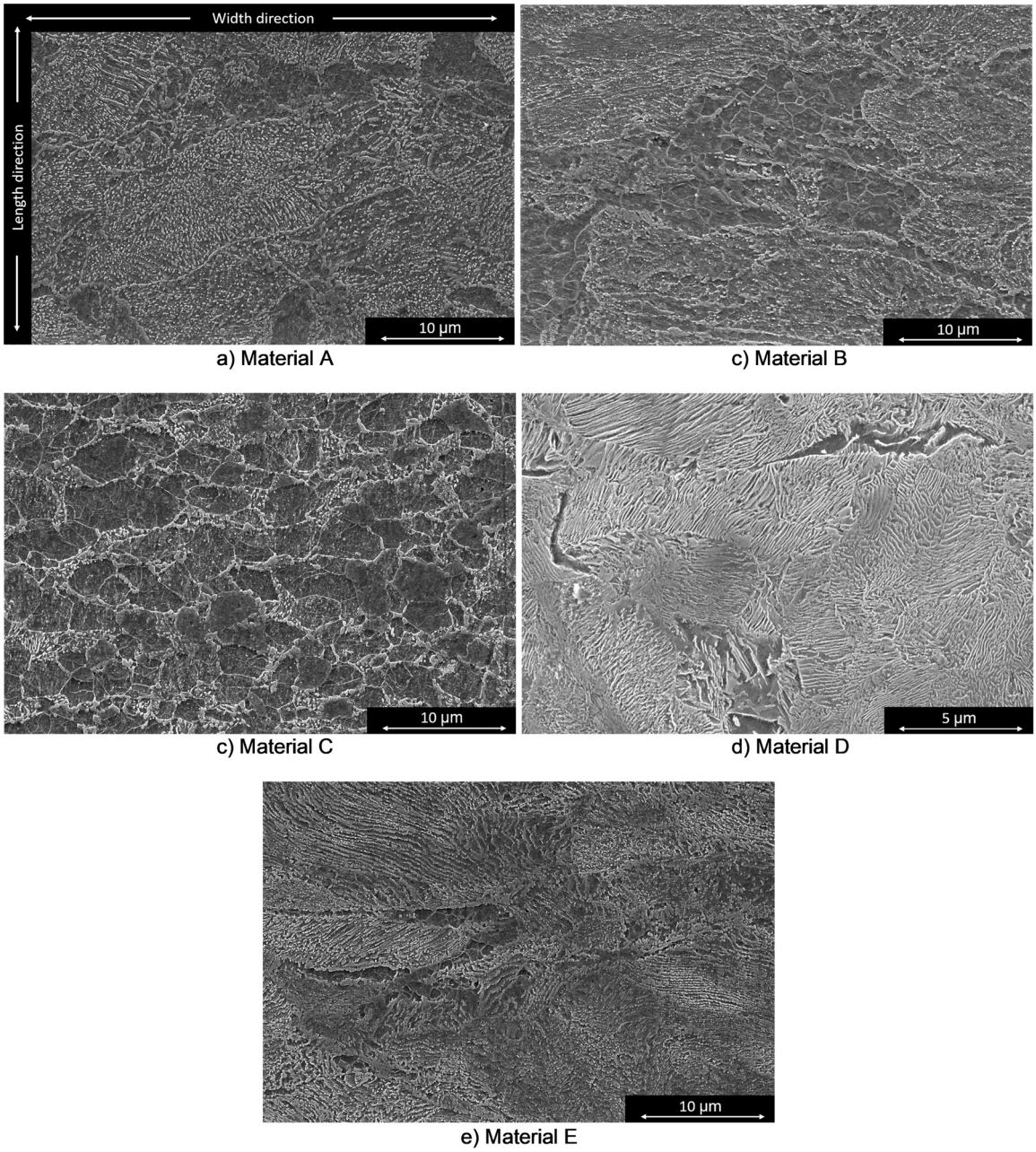

Fig. 1. SEM images in width-length plane for the materials included in the test program.

microstructure. Several theories have been proposed to explain the mechanism, including the internal pressure theory [10], hydride formation [11], hydrogen enhanced strain-induced vacancies [12], hydrogen enhanced localized plasticity [13,14], hydrogen enhanced decohesion [15] and the defactant theory [16]. The elemental hydrogen in the steel can exist in lattice and in microstructural sites with a higher affinity for hydrogen than the lattice. Voids, vacancies, interstitials, phase boundaries, grain boundaries, dislocations and some intermetallic particles like TiC and MnS are all microstructural features that can act as hydrogen traps in steels [17]. The hydrogen uptake in steels at open circuit potential (OCP) depends on both the steel microstructure, the environment, and the surface condition. The cathodic corrosion reactions and their reaction rates affect the quantity of hydrogen reacting on the surface, but the presence of hydrogen recombination poisons, for example the elements S, P and Pb, affect the rate of hydrogen recombination vs. hydrogen absorption [18]. The amount of absorbed hydrogen is also dependent on where the cathodic reaction is taking place. Pure CO_2 corrosion of steels can start with the selective dissolution of ferrite phase while the Fe_3C structure is retained [19–21]. The Fe_3C is conductive and is mainly a cathodic site during CO_2 corrosion, and as the Fe_3C surface area increases, the dissolution of ferrite accelerates [19,22]. The retained Fe_3C can form a thick porous layer, and if the pH and the concentration of dissolved iron are sufficiently high, iron carbonate can precipitate in the Fe_3C layer and significantly reduce the corrosion rate [19,20]. Silva et al. [21] conducted electrochemical hydrogen permeation tests on pre-corroded steel samples with Fe_3C or $FeCO_3$ rich layers. The sample with the $FeCO_3$ layer had twice as much hydrogen as a reference wet-ground sample without any surface layer, while the sample with a Fe_3C rich surface layer had five times more hydrogen than the wet-ground sample. The formation of a retained Fe_3C layer may also lead to an internal acidification in the layer which prevents later formation of $FeCO_3$ in contact with the metal [23]. Plennevaux et al. [24] measured the hydrogen uptake in a sour service pipe steel exposed to 0.1 mol L^{-1} potassium perchlorate ($KClO_4$) and various

Table 1
Cementite volume fractions (f) and chemical compositions of the wire materials. Elements that were not detected for a particular material are labeled with N.D.

Material	f [-]	C [wt%]	Si [wt%]	S [wt%]	P [wt%]	Mn [wt%]	Ni [wt%]	Cr [wt%]	Al [wt%]
A	0.077	0.501	0.247	0.002	0.003	0.604	0.001	0.011	0.031
B	0.043	0.282	0.223	0.010	0.006	0.733	0.010	0.003	0.035
C	0.054	0.353	0.194	0.007	0.009	0.678	0.013	0.003	0.042
D	0.127	0.830	0.331	0.005	0.005	0.683	0.005	0.002	0.041
E	0.095	0.618	0.225	0.002	0.007	0.729	0.009	0.032	0.037
Material	V [wt%]	Pb [wt%]	N [wt%]	Ti [wt%]	Sn [wt%]	Cu [wt%]	Co [wt%]	Mo [wt%]	B [wt%]
A	0.036	0.050	0.009	$< 10^{-4}$	N.D.	N.D.	N.D.	0.001	$< 10^{-4}$
B	0.001	0.065	0.020	0.002	N.D.	$< 10^{-4}$	$< 10^{-4}$	0.001	$< 10^{-4}$
C	0.002	0.065	0.219	0.002	$< 10^{-3}$	0.001	N.D.	0.001	$< 10^{-4}$
D	0.050	0.065	0.099	0.004	0.001	$< 10^{-4}$	N.D.	0.002	$< 10^{-3}$
E	0.001	0.050	0.014	$< 10^{-4}$	N.D.	N.D.	N.D.	$< 10^{-3}$	$< 10^{-4}$

partial pressures of N_2, CO_2 and H_2S while cathodically polarized. They found that the hydrogen uptake increased with the H_2S pressure and was higher for H_2S in CO_2 than H_2S in N_2. Wallaert et al. [25] measured the hydrogen content of two steels exposed to NACE test TM0284 solution A over four weeks by hot extraction. The concentration of diffusible hydrogen peaked within 5 days of exposure, then decreased to less than half of the peak value within 20 days. The corrosion currents increased with time and the decrease in hydrogen concentration was attributed to the formation of a double layer of FeS corrosion products where S^{2-} and HS^- were migrating to the steel surface to form the inner layer. Huang et al. [26] performed electrochemical permeation tests on pre-corroded steel samples in a solution containing H_2S. The results showed that crystalline FeS formed at low pH and low H_2S concentrations, while mackinawite formation was promoted with the increase of H_2S concentration (from 0.2 to 20 mM) and/or pH (from 3.5 to 5.5). The blocking effect of the surface film on hydrogen permeation increased with increasing H_2S concentration and reduced pH value. Zhou et al. [27] conducted several electrochemical hydrogen permeation tests for an X80 pipeline steel exposed to pure H_2S, pure CO_2 and several H_2S/CO_2 partial pressures to study the permeation behavior and effect of corrosion products on hydrogen permeation. They observed different hydrogen permeation behaviors and concluded that these were controlled by the mutual coupling of the hydrogen promoting effect of H_2S and CO_2, the corrosion products, and the hydrogen evolution during the corrosion reaction.

This work investigates the hydrogen uptake of carbon steels exposed under upset conditions not giving the high supersaturation of dissolved corrosion products required for protective film formation [28,29]. Five carbon steel tensile armor wires for flexible pipes with different microstructures were exposed to modified artificial seawater (ASTM D1141–90) bubbled with CO_2 and H_2S at OCP. The experiments were conducted with an electrochemical permeation cell similar to the design by Devanathan and Stachurski [30]. The wires were first exposed to 0.2 bar CO_2 and 1 bar CO_2, before H_2S was added and the partial pressure of H_2S was varied in steps. This gave several hydrogen permeation transients that showed how the changes in surface condition affect the hydrogen uptake. The electrolyte was continuously replaced to maintain a low concentration of dissolved iron in the electrolyte. The corrosion products on the sample surface were characterized by scanning electron microscopy (SEM), x-ray diffraction (XRD) and energy-dispersive spectroscopy (EDS), and the samples were stripped to measure the weight of corrosion products attached to the surfaces. To provide more insight in the interplay between steel microstructure, hydrogen uptake, corrosion rates and corrosion products, the results are compared with the hydrogen uptakes measured during cathodic polarization in previous work [31]. In [31], the hydrogen uptake of the same wire materials was investigated with hydrogen introduced by cathodic polarization to -12 mA cm^{-2} in deaerated 0.1 M NaOH at 25 °C.

2. Experimental

2.1. Materials

Five different tensile armor wire steels were tested. The wires were identified by letters A to E. The wire materials were qualified according to API 17 J Specification for Unbonded Flexible pipe [32], but are designed for different operating conditions. Not all the wires were qualified for exposure to H_2S (referred as sour service). The wires were 3 mm thick with widths from 9 to 12 mm and were taken from coil. Fig. 1 shows SEM images of the materials in the width-length plane. The microstructures of the materials consist of ferrite and pearlite. The cementite volume fraction, f, was estimated with the lever rule, assuming all C is located in cementite. The chemical compositions and f are given in Table 1. A description of the degree of plastic deformation, grain size, cementite morphologies and mechanical properties are given in Table 2. The microstructures of the materials are complex, and the positions of the grain boundaries are not always easy to find. The grain size is therefore described by the largest well-defined grains observed rather than the average grain size, and the grains of ferrite and cementite were evaluated separately. The yield strength (YS), ultimate tensile

Table 2
Mechanical and microstructural properties of the wire materials.

Material	Extent of plastic deformation			Cementite morphology		
A	Some deformation.			Globular, partly lamellar		
B	Pearlite deformed. Some banding of ferrite.			Globular		
C	Some banding and deformation.			Globular		
D	Highly deformed grains.			Lamellar		
E	Pearlite deformed. Some banding of ferrite.			Globular, partly lamellar		
Material	Estimated grain size[a]		Hardness [HV_{10}]	YS [MPa]	UTS [MPa]	Ep [-]
	Ferrite [μm]	Cementite [μm]				
A	≤ 14	≤ 36	331 ± 14	871	1009	0.115
B	≤ 10	≤ 28	290 ± 10	805	847	0.157
C	≤ 20	≤ 14	257 ± 4	616	744	0.152
D	≤ 7	≤ 24	453 ± 16	1408	1622	0.094
E	≤ 3	≤ 22	386 ± 8	1097	1260	0.108

[a] Max grain size.

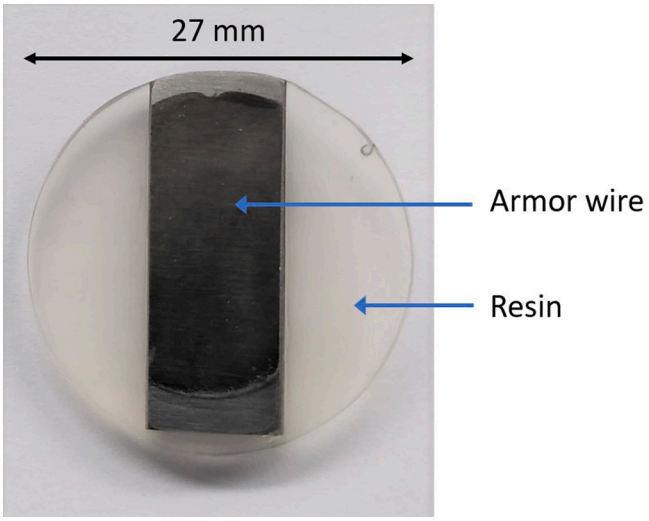

Fig. 2. Embedded sample for electrochemical hydrogen permeation experiments.

strength (UTS) and plastic strain-to-failure (Ep) were measured with tensile Slow Strain Rate Tests (SSRT) using a strain rate of 10^{-6} s^{-1}. The plastic strain-to-failure was determined in agreement with NACE Standard TM0198–2016 [33]. Hardness was measured in the cross-sections of the samples with a ZwickRoell ZHV30 Vickers hardness tester using condition HV10.

2.2. Sample preparation

The wires were coiled, and the most bent wires were straightened with a roller straightener before cutting. The wires were cut in ~2.8 cm long pieces, which were ground with SiC paper on both sides until flat, washed in acetone and sonicated in ethanol. The corners of the wire pieces were also ground so the wire pieces could fit a mounting cup with 3 cm diameter. The pieces were then embedded in a light-curing resin (Technovit® LC 2000, mixed with the additive "Inside Cure") to form a disc-shaped sample, see Fig. 2. When installed in the permeation cell, the exposed area is 1.72 cm^2 for the samples made with the narrowest wire materials and 2.26 cm^2 for the samples with the widest wire materials. Ideally, the permeation test samples should have a circular exposed area which fulfills minimum 10:1 radius-to-thickness ratio, to guarantee one-dimensional diffusion through the thickness [34,35]. However, other sample configurations are accepted if there are limitations in material form [34]. After mounting, the two sides were ground with European grit P1200 SiC paper and the sample heated in a heating cabinet overnight at 120 °C. Sites with weak adhesion between the steel and polymer were visible after heating and only the defect-free samples were tested. To ensure fast oxidation of hydrogen on the detection side of the sample, this side was coated with Pd. The coating was applied by electrodeposition with the procedure proposed by Bruzzoni [36] and further developed by Husby et al. [37]. After Pd-coating, the samples were heated to 120 °C in a heating cabinet for minimum 16 h to remove any hydrogen absorbed during the Pd-coating process. The sample surface without Pd-coating was ground with European grit P1000 SiC paper, rinsed in isopropanol and dried in air stream within an hour before the start of the electrochemical hydrogen permeation experiments. The final sample thicknesses ranged from 2.64 to 2.92 mm.

2.3. Chemicals and gases

The permeation cell consists of two compartments: one where the corrosive environment is created, and one where the hydrogen that permeates through the sample is detected. The corrosion compartment was filled with modified ASTM D1141–90 electrolyte. The electrolyte was prepared with analysis grade salts and distilled water, but without $CaCl_2$, NaF and KBr. The electrolyte in the detection compartment was 0.1 M NaOH which was made with analysis grade NaOH. CO_2 and N_2 gas with 99.999% purity were used. The H_2S gas was mixed in house from 99.999% purity CO_2 and 99.8% purity H_2S and the concentration was determined by gas chromatography. The gases were mixed to the desired composition using mass flow controllers. The gas flow into the corrosion compartment was ca. 600 mL h^{-1}.

2.4. Procedure

The steel sample was placed in the sample holder and clamped with gaskets between two glass cells, as shown in Fig. 3. A screw in the sample holder ensured electrical contact between the sample and the potentiostats used for corrosion measurements and hydrogen detection. The tests were conducted at ambient pressure and the temperature was kept at 25 °C by circulation of water through the double walls of the permeation cell. The tests started with stabilization of the detection side of the sample for ~72 h. The detection compartment contained 0.1 M NaOH bubbled with N_2 and polarized to + 540 mV vs. the normal hydrogen electrode (NHE). The corrosion chamber was fed with N_2 gas

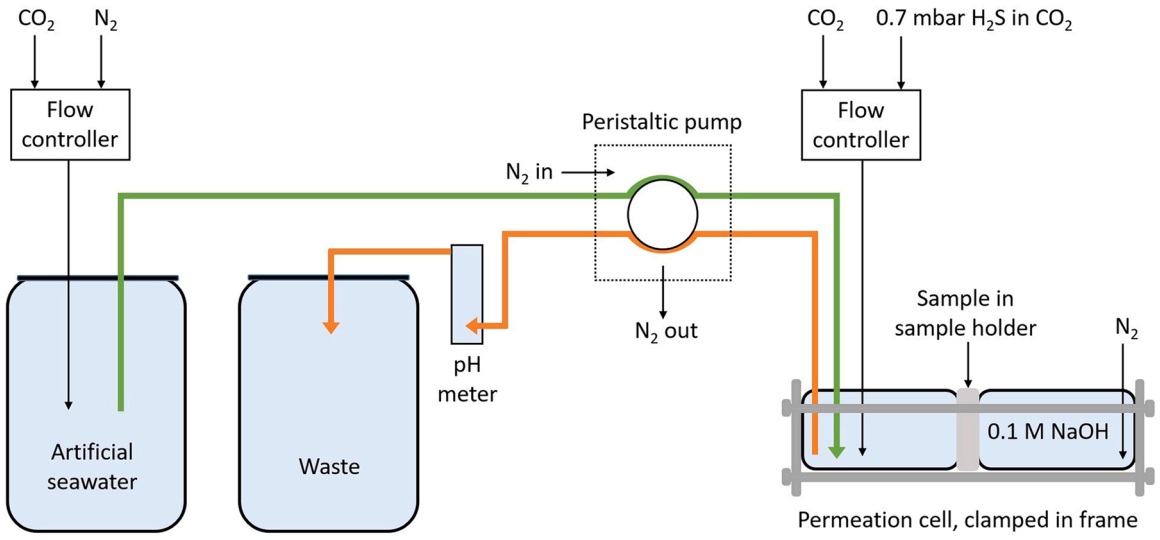

Fig. 3. Schematic of the test setup.

Table 3
Conditions in the corrosion compartment.

Step	0	1	2	3	4	5	6	7	8
Duration	~	~	~	~	~	~	~	~	~
[h]	72	48	48	48	48	72	24[a]	24	24[b]
Electrolyte	–	Yes	Yes	Yes	Yes	Yes	Yes	Yes	Yes
p_{N2} [bar]	1	0.8	–	–	–	–	–	–	–
p_{CO2} [bar]	–	0.2	1	1	1	1	1	1	1
p_{H2S} [mbar]	–	–	–	0.1	0.2	0.4	0.7	0.2	0.1

[a] For Material D, step 6 was lengthened by a day to compensate for a period of clogged liquid and gas supply in step 5.
[b] For Material A, step 8 lasted 2 days due to scheduling issues.

during the stabilization of the detection side of the sample. After ~72 h of stabilization, the electrolyte bubbled with 0.2 bar CO_2 and 0.8 bar N_2 was added to the corrosion compartment. The solution was continuously refreshed by pumping electrolyte from a feeding unit and pumping out used solution to a waste container. The flow rate of electrolyte was 25–35 mL h^{-1}. After ~48 h, the CO_2 pressure was increased to 1 bar CO_2 and kept for ~48 h before 0.1 mbar H_2S was added to the gas stream. The CO_2 pressure during the H_2S exposure was 1 bar, and the H_2S partial pressure was first increased stepwise from 0.1 mbar to 0.7 mbar, then decreased to 0.1 mbar. The gas composition in the corrosion compartment is shown in Table 3. The gas pressures were adjusted without stopping the flow of gas into the corrosion compartment. The pH was measured in the electrolyte that was pumped out of the corrosion compartment and the waste electrolyte was collected for measuring the concentration of Fe^{2+} in the solution. A controlled amount of 1 M HCl (ca. 13% of the expected waste volume) was added to the waste containers before the waste collection started to prevent oxidation and precipitation of the dissolved iron. Aliquots of the collected waste were added to a developer solution and the dissolved iron content was determined by spectrophotometric analysis. Linear polarization resistance (LPR) was measured to estimate the corrosion rate. In addition, OCP was measured.

2.5. Electrochemical measurements

The polarization of the detection side of the sample was conducted in a 3-electrode set-up with the sample as working electrode, a platinum wire as counter electrode, and a mercury-mercurous electrode (MME), $Hg/HgSO_4/SO_4^{2-}$ sat. K_2SO_4, as reference. The MME electrode has a potential of + 650 mV vs. NHE. Two Interface 1010E potentiostats (Gamry Instruments®) were used for the experiments: One for polarization of the detection side and one for running linear polarization resistance (LPR) measurements and electrochemical impedance spectroscopy (EIS) on the corrosion side of the sample. The LPR and EIS measurements were performed in a 3-electrode set-up with the sample as working electrode, a platinum wire as counter electrode, and Ag/AgCl (3 M KCl) as reference electrode. The LPR scans were conducted every 30 min at 0.1 mV s^{-1}, from − 5 to + 5 mV relative to the open circuit potential (OCP). The corrosion current density was calculated with the Stern-Geary equation:

$$i_{corr} = \frac{B}{RpA} \tag{5}$$

where A is the sample area exposed in the corrosion compartment, B is the Stern-Geary constant which was set to 20 mV (the value was empirically chosen based on previous experience and tests conducted in a similar environment), and Rp is the polarization resistance, defined by the ratio between the variation in potential (E) and current (I):

$$R_p = \frac{\Delta E}{\Delta I} \tag{6}$$

The polarization measurements were corrected for the solution resistance (R_s) which was determined by EIS. The frequency range was 0.01–10000 Hz, the AC voltage was 10 mV vs. OCP and 6 points per decade were recorded.

2.6. Surface analysis / postmortem analysis of samples

After the permeation test, the samples were retrieved from the permeation cell, cleaned in isopropanol and dried in air stream. The samples were examined by SEM and the chemical composition of the corrosion products was determined by EDS and XRD. A carbon tape was then lightly attached to the surfaces and removed in order to analyze the corrosion products that remained on the surface. The samples were weighed after the test, after attachment of carbon tape and after stripping to estimate the weight of corrosion products attached to the surface, i.e. the film weight. The stripping of corrosion products was done by exposing only the corroded side of the sample to modified Clarke's solution for ca. 1 min, then quickly rinsing with distilled water, isopropanol and drying in air stream.

2.7. Calculation of hydrogen uptake

During steady-state permeation, it is assumed that the hydrogen traps are occupied and that the reversibly trapped hydrogen is in equilibrium with the lattice hydrogen. Cementite is considered to be both an obstacle for hydrogen diffusion and a contributor to increased hydrogen uptake by trapping on the ferrite-cementite interfaces [38–40]. The diffusion of hydrogen inside the cementite phase can therefore be neglected, which means the diffusion of hydrogen in lattice during steady state is determined mainly by the theoretical diffusion coefficient of ferrite, D_l. Considering an even amount of hydrogen over the subsurface of the hydrogen entry side, the steady-state flux of hydrogen, J_{SS}, will be

$$J_{SS} = \frac{D_l C_0^{av}}{L} \tag{7}$$

where L is the length of the diffusion path and C_0^{av} is the average lattice hydrogen concentration on the subsurface of the hydrogen entry side. In the temperature range − 40–80 °C, D_l is given by [41].

$$D_l = 7.23 \times 10^{-8} \exp\left(-\frac{Q}{RT}\right) \text{ m}^2\text{s}^{-1} \tag{8}$$

where $Q = 5.69$ kJ mol^{-1} and R is the gas constant 8.314 J K^{-1} mol^{-1}. This gives $D_l = 7.28 \times 10^{-5}$ cm^2 s^{-1} at 25 °C. When any obstacles to hydrogen diffusion have negligible effect on the diffusion path, L is equal to the sample thickness. In our previous work [31], a tortuosity factor, τ, was estimated for the five materials. This factor was defined as the true length of the diffusion path divided by the sample thickness, as suggested by Forot et al. [42]. Since the hydrogen is expected to exist in traps and ferrite lattice, with a negligible amount of hydrogen inside the cementite phase, the subsurface hydrogen concentration can be adjusted to take the fraction of cementite, f, into account [43].

$$C_0^{fe} = \frac{C_0^{av}}{1-f} \tag{9}$$

To calculate the concentration of diffusible hydrogen, i.e. hydrogen in lattice and reversible sites, C_{0R}, Eq. (7) can be reformulated with the effective diffusion coefficient of hydrogen, D_{eff} [35].

$$C_{0R} = \frac{J_{SS} L}{D_{eff}} \tag{10}$$

During corrosion, the boundary conditions on the hydrogen entry side are changing over time, making the estimation of D_{eff} challenging. The hydrogen uptakes are therefore estimated using the effective diffusion coefficients determined in previous work [31] from the decay transients measured after 72 h of galvanostatic charging to

Table 4
Effective diffusion coefficients and tortuosity factors determined in previous work [31]. The tortuosity factors are given with their standard deviations.

Material	D_{eff} [cm^2 s^{-1}]	τ [-]
A	1.19×10^{-6}	1.122 ± 0.036
B	7.55×10^{-7}	1.055 ± 0.010
C	1.81×10^{-6}	1.056 ± 0.022
D	6.62×10^{-7}	1.669 ± 0.266
E	9.73×10^{-7}	1.158 ± 0.015

− 12 mA cm^{-2} in 0.1 M NaOH. The effective diffusion coefficients and the tortuosity factors are given in Table 4. The estimated tortuosity factors were taken into account when calculating the effective diffusion coefficients and the difference between D_{eff} and D_l should therefore only reflect the reduction of diffusivity due to trapping of hydrogen.

The changing boundary conditions can also prevent a steady state to be reached during the tests. The equations for calculation of hydrogen uptake, (7), (9) and (10) are valid at steady state, but sometimes the permeation flux is increasing or decreasing with time instead of staying steady. In these cases, the steady state permeation flux may be replaced with a peak permeation flux [44] or the permeation flux after a certain exposure period [37].

3. Results

3.1. Corrosion parameters measured on the hydrogen entry side

3.1.1. Analysis of corroded surfaces

The XRD analyses showed peaks for Fe_3C for all materials, but iron carbonate and sulfides were not detected, see Fig. 4. Retained carbides were not easily identified in the first examination of the corroded surfaces in SEM, but after removal of the loose corrosion products by attaching and removing a carbon tape, it was evident that retained carbides were present on all the surfaces, see Fig. 5. Fe, C and O were the main elements detected by EDS in the corrosion products. Table 5 shows the film weight and the EDS analyses on the corroded surfaces after the loose corrosion products were removed with a carbon tape. The S content in the corrosion products was lowest for materials A and C, 0.4 at%. The highest S content was found for material D, 1.0 at%. The materials' rank of film weight from lowest to highest follows the rank in carbon content, B < C < A < E < D. Material B was tested twice, and the two tests are denoted B1 and B2. B1 was conducted with a sample that had been previously used in a permeation experiment whereas B2 was conducted with a fresh sample like in the other tests. For Material B, Fig. 5 shows the sample from test B2, but the sample from test B1 displayed the same characteristics.

3.2. pH and content of dissolved iron

The dissolved iron content in the collected waste and the pH measured continuously in the electrolyte pumped out of the corrosion compartment are shown in Table 6. The iron content was highest during step 2, where the sample was exposed to 1 bar CO_2. This coincides with the time of highest corrosion rate, see Fig. 6. The pH was highest during exposure to 0.2 bar CO_2 and was relatively stable during the steps with 1 bar CO_2 and varying partial pressure of H_2S.

3.2.1. Corrosion rates and OCP

The corrosion rates measured by LPR during step 1–8 of the permeation tests are given in Fig. 6. A clogging incident of the tubes supplying both liquid and gas to the corrosion compartment occurred during the test for Material D about 200 h after the electrolyte was added to in the corrosion compartment (step 5). The bubbling in the compartment stopped completely and this resulted in increased corrosion rate and decreased hydrogen permeation flux, probably due to a reducing concentration of H_2S in the cell with time. This issue was fixed around 250 h of exposure and the pH reached a similar level as before the incident. Step 6 (see Table 3) was extended by ~24 h in this test to allow a steady-state permeation flux to be reached.

In step 1, the 0.2 bar CO_2 exposure period, the corrosion rates were about 0.7 mm y^{-1} or lower, and relatively stable. The difference in corrosion rate during this step was sometimes larger for the two samples of Material B than it was for two samples of different materials. The same holds for the OCP measurements during this step, see Fig. 7. During the 1 bar CO_2 exposure, the corrosion rates increased to over 1 mm y^{-1} during all the tests except B2. For materials A, C, D and E, the corrosion rates increased with time during this step of the permeation test, but for Material B the corrosion rate was relatively stable or slightly decreasing. The corrosion rates of the lamellar material, D, increased more rapidly than the corrosion rates of materials A, C and E. The OCP level was also increasing for all the materials during the 1 bar CO_2 step of the permeation test.

H_2S exposure started ~96 h after the electrolyte was added in the corrosion compartment, and the corrosion rates decreased immediately. The increased corrosion rate for Material D during the 0.4 mbar H_2S step of the test was related to the clogging of the tubes for supplying gas and electrolyte directly into the corrosion compartment.

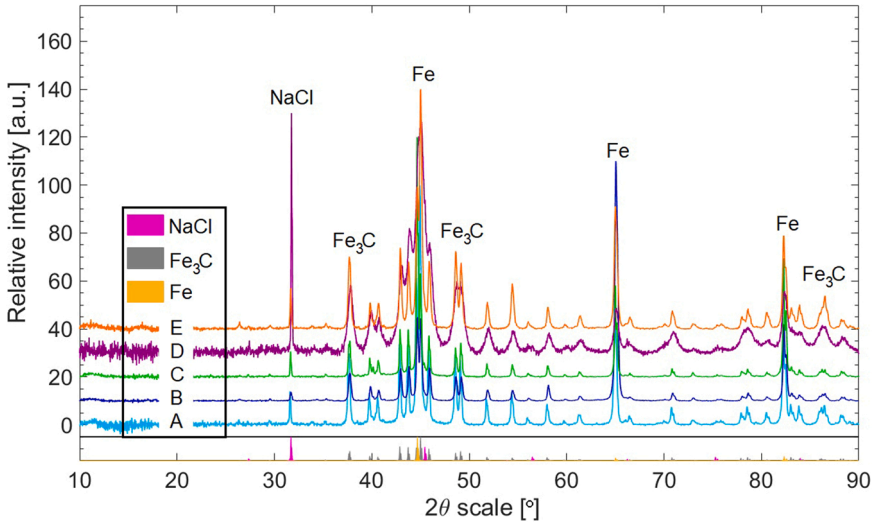

Fig. 4. Relative intensity of XRD signals from the corroded surfaces of the tested samples.

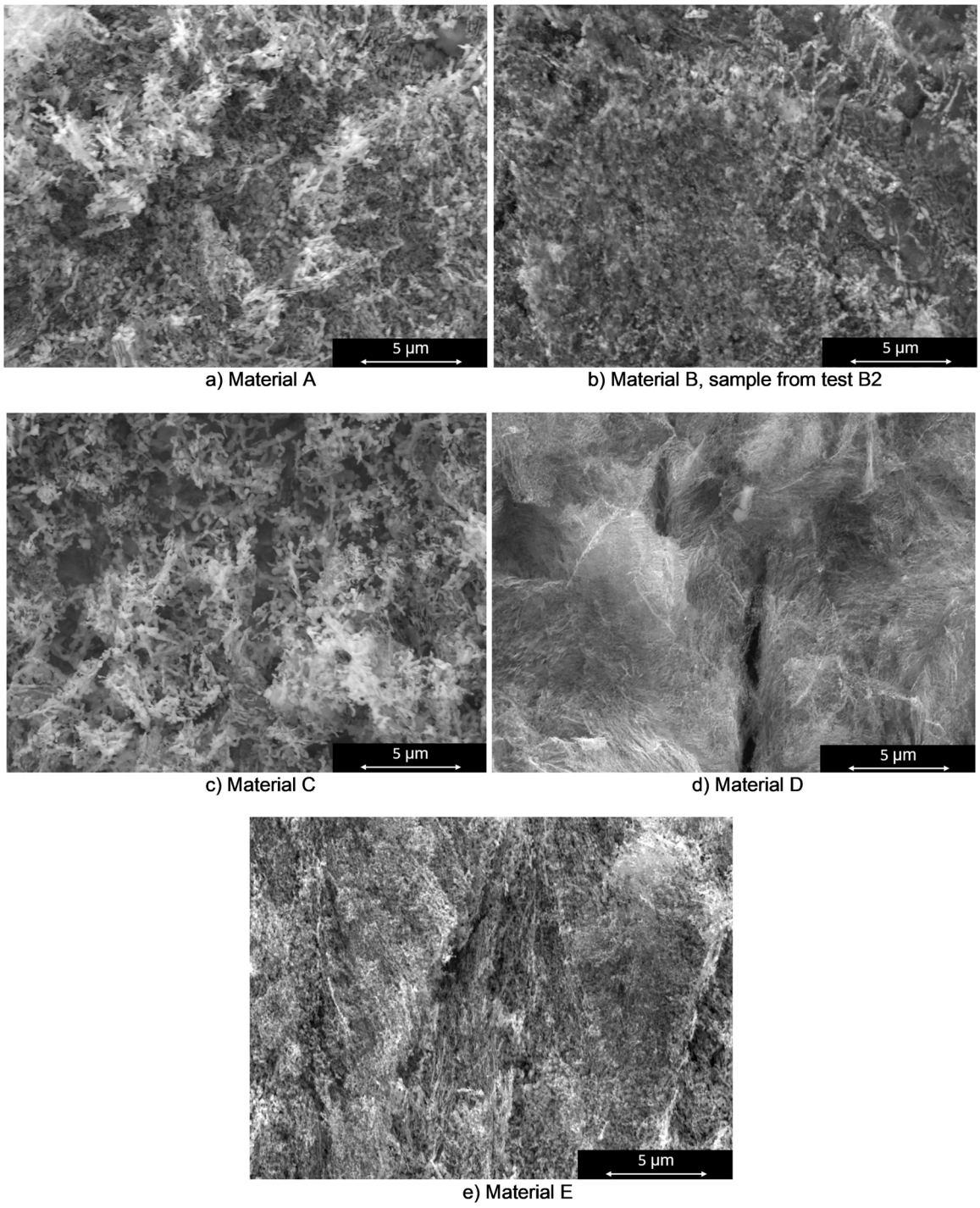

Fig. 5. Surface exposed after removal of corrosion products with carbon tape.

Table 5
EDS analyses on the corroded surfaces after removal of loose corrosion products with carbon tape and film weight measured by stripping the samples.

Material	C [at%]	O [at%]	S [at%]	Fe [at%]	Other [at%]	Film weight [mg cm^{-2}]
A	35.0 ± 9.2	9.6 ± 1.7	0.4 ± 0.1	52.2 ± 10.7	2.8	2.65
B (test B2)	27.6 ± 5.1	24.9 ± 7.2	0.8 ± 0.1	42.9 ± 7.7	3.7	0.84
C	35.3 ± 11.1	7.6 ± 3.3	0.4 ± 0.1	54.0 ± 14.2	2.7	2.27
D	33.7 ± 3.6	19.5 ± 2.5	1.0 ± 0.1	44.5 ± 5.0	1.3	4.18
E	32.5 ± 3.6	15.3 ± 1.7	0.7 ± 0.1	49.9 ± 4.0	1.6	2.74

Table 6
Dissolved iron content and pH measured in the electrolyte disposed from the corrosion compartment.

Step	1	2	3	4	5	6	7	8
pH [-]	5.6–5.9	4.9–5.2	4.9–5.2	4.9–5.2	4.9–5.2[a]	4.9–5.2	4.9–5.2	4.9–5.2
Fe^{2+} [ppm]	1.1–2.4	2.7–9.5	1.8–8.9	1.4–3.4	1.5–3.6	1.5–3.8	1.5–3.1	1.3–3.3

[a] Material D had a period of clogged liquid and gas supply in step 5 which interfered with the pH measurements during this step. The pH measurements of Material D during step 5 are therefore not included.

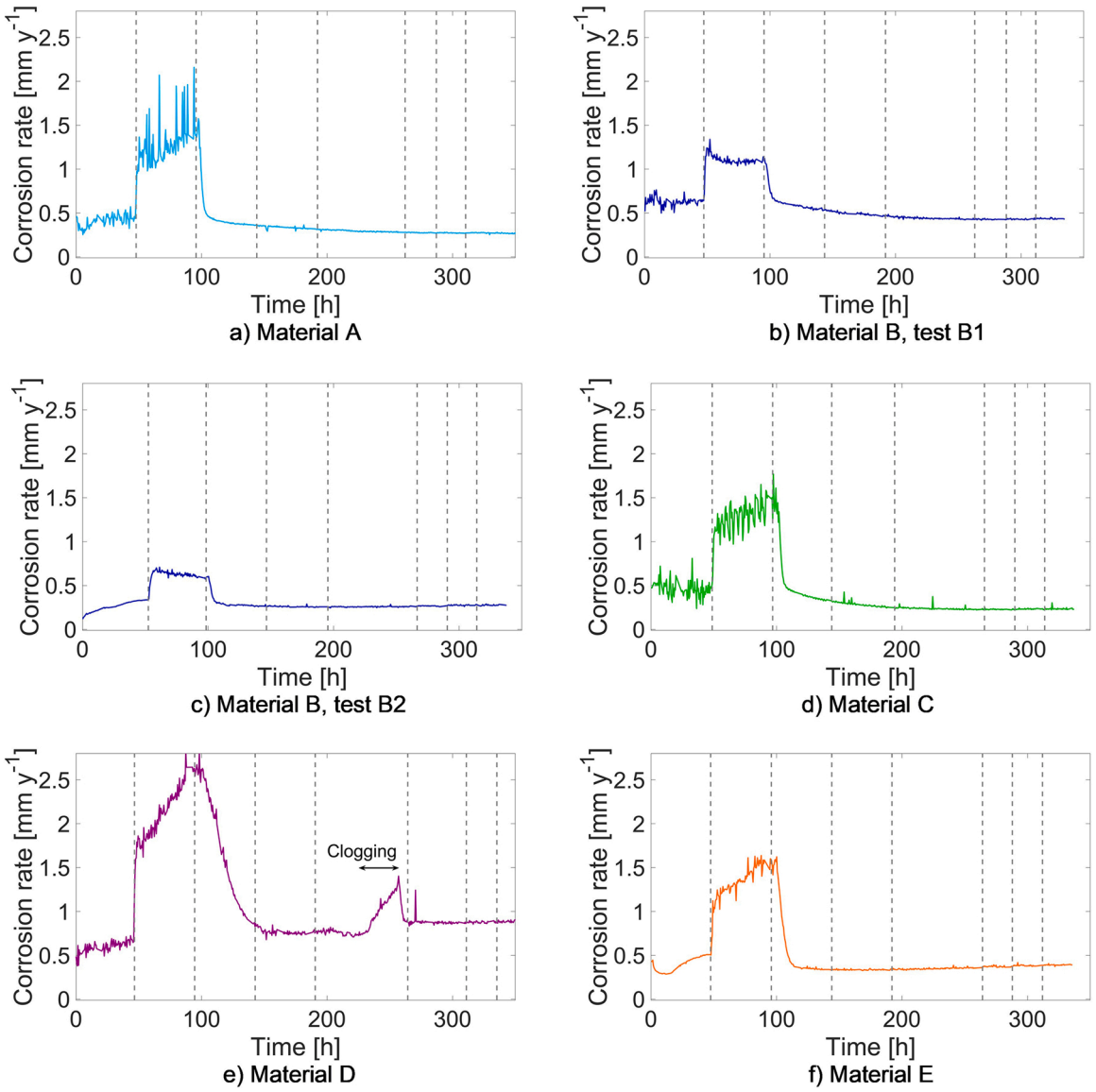

Fig. 6. LPR corrosion rates vs. time after the electrolyte was added in the corrosion compartment. The dashed lines mark the steps with different p_{CO2} and p_{H2S}, as described in Table 3.

3.3. Hydrogen permeation and uptake

The permeation current measured on the detection side of the sample while the corrosion side was exposed to the test solution is given for each material in Fig. 8. Materials A, C, D and E had a lower permeation current the second time the H_2S pressure was set to 0.1 mbar and 0.2 mbar, compared to the first time. In contrast, both tests for Material B had a higher hydrogen uptake the second time the corrosion compartment was supplied with 0.1 mbar and 0.2 mbar H_2S. When the hydrogen permeation flux increased in response to a change in CO_2 or H_2S pressure, the current increased until it reached a plateau or a peak. The time until a peak or plateau is reached depends on the real diffusion length, which is longer for materials with a high tortuosity factor. Material D has lamellar carbides and a high tortuosity factor and did not reach a plateau or peak for all the steps in the test. The plateaus and peaks were typically reached towards the end of the steps for this material if a plateau or peak was reached at all. For steps 1–6, the hydrogen uptakes were estimated for each step where a plateau or peak permeation current was reached in the test, using the permeation flux measured in the last hour of the step. For steps 7 and 8, the hydrogen uptakes were estimated from the plateau currents for the tests where a plateau was observed for these steps.

The hydrogen uptakes of the materials are shown in Figs. 9 and 10.

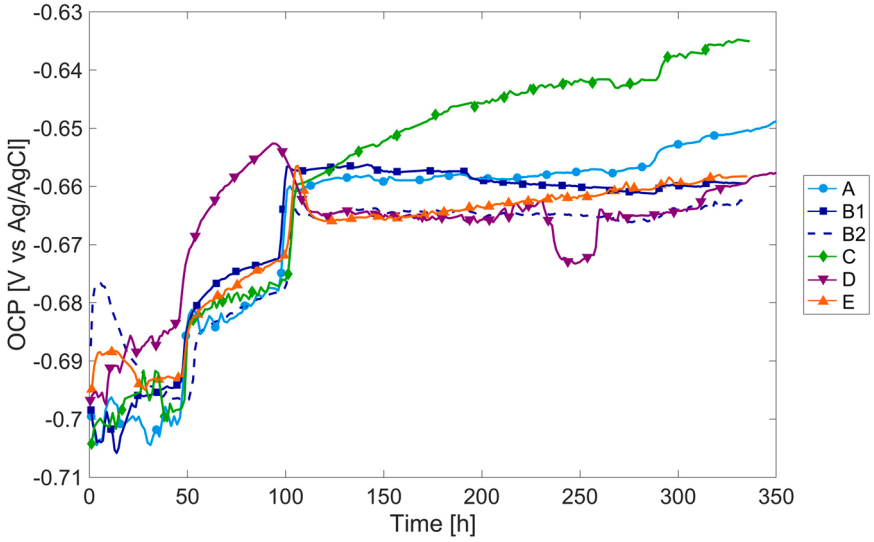

Fig. 7. OCP on the corrosion side of the sample vs. time after the electrolyte was added in the corrosion compartment.

An extra test for Material E, denoted E2, is included in the evaluation of hydrogen uptake during pure CO_2 corrosion. This test followed steps 0, 1 and 2 of the test program in Table 3, but an error occurred in the H_2S part, and those results are therefore not included. The deviation of hydrogen uptake for the two tests of Material B was 18% and 19% for the pure CO_2 steps and below 4% for the steps in H_2S environment.

During pure CO_2 corrosion, the hydrogen uptake could not be measured for the lamellar material, D. The high tortuosity of lamellar materials leads to both a lower permeation current, and a longer time-lag between a change in subsurface hydrogen concentration and corresponding change in permeation current on the hydrogen detection side. This explains the absence of a clear increase in permeation current during the CO_2 exposure for Material D. Material B had the highest C_{0R} measured during pure CO_2 corrosion (step 1 and 2 in Table 3), more than twice as high as the hydrogen uptakes of materials A, C and E. The hydrogen concentration in ferrite lattice was also higher for Material B than the other materials with globular Fe_3C. The repetition of hydrogen permeation tests for materials B and E show that the method was not accurate enough to measure the difference in hydrogen uptakes for materials A, C and E during pure CO_2 corrosion with confidence.

The hydrogen uptake in reversible traps during the H_2S exposure was highest for Material D and lowest for Material C, see Fig. 10. Materials A, E and B had the second, third and fourth lowest C_{0R} respectively. For the two last steps of the H_2S exposure, the materials had the same rank in C_0^{fe} and C_{0R}, but the hydrogen uptake was only measured for the materials with globular Fe_3C in these steps since a plateau current was not reached for the lamellar material, D.

The hydrogen uptakes measured for the same materials under exposure to 0.1 M NaOH and cathodic polarization to $-$ 12 mA cm^{-2} at 25 °C in previous work [31] are shown in Table 7. The hydrogen uptakes in Table 7 were estimated with the diffusion coefficients and tortuosity factors in Table 4. All the materials had lower hydrogen uptakes when exposed to modified artificial seawater with CO_2 and H_2S than during cathodic polarization in 0.1 M NaOH, but the difference is more significant for some materials than others.

4. Discussion

4.1. Corrosion products

The XRD results and images of the corroded surfaces in Fig. 5 show that all the surfaces have retained carbides which are exposed when iron is preferentially dissolved from the ferrite phase. $FeCO_3$ was not detected by the XRD, and the oxygen detected by EDS is therefore expected to originate mainly from oxides present on the surface before the electrolyte was added or oxygen that has reacted with the surface after the test. The selective dissolution of ferrite phase during pure CO_2 corrosion of steels is associated with an increase in corrosion rate and OCP with time due to the increasing surface area of retained Fe_3C [20,21]. This was seen for all the materials at 1 bar CO_2 exposure (step 2), except for Material B which had a relatively stable or declining corrosion rate. The surface of Material B may therefore have entered a more stable condition than the other materials at this stage. The carbides in Material B have a fine distribution and the carbide fraction is smaller than the carbide fraction of the other materials. Possibly, the amount of retained Fe_3C on the surface of Material B reached an equilibrium where the outer parts of the Fe_3C network were losing their electrical contact to the steel at the same rate as new Fe_3C was being exposed on the surface. The most rapidly increasing corrosion rates were found for the lamellar Material D, which has better foundation for increasing the Fe_3C surface area due to the continuous nature of the lamellar phase.

Small amounts of S (0.4–1.0 at%) were detected on all the corroded surfaces by EDS, but crystalline species containing S were not detected by XRD. In aqueous solutions containing H_2S, mackinawite is the major constituent of precipitated FeS. Mackinawite can precipitate as nano-sized platelets which are difficult to detect with classical XRD, since this technique relies on many repetitions of a periodic lattice. This has led to wrongful characterization of mackinawite as amorphous FeS [45]. The S detected on the corroded surfaces is therefore expected to be in the form of mackinawite, despite the lack of mackinawite XRD signal. For low H_2S concentrations ($\leq$ 340 ppm) in aqueous CO_2 environment, mackinawite has been observed to reduce the corrosion rate [46], and this was also observed in our experiments. The reduced corrosion rates in [46] were attributed to mackinawite acting as a charge-transfer barrier rather than a mass-transfer barrier.

4.2. Hydrogen uptake during pure CO_2 corrosion

During pure CO_2 corrosion, the C_{0R} of Material B was more than twice as high as the C_{0R} of Material A, C and E, and the C_0^{fe} was also significantly higher for Material B. The hydrogen uptake in Material D during pure CO_2 corrosion could not be determined and is therefore not discussed. When cathodically polarized in 0.1 M NaOH, the hydrogen uptake for materials B and E were twice as high as the hydrogen uptakes of materials A and C. The difference in hydrogen uptake under cathodic polarization and in CO_2 environment indicates that the hydrogen uptake

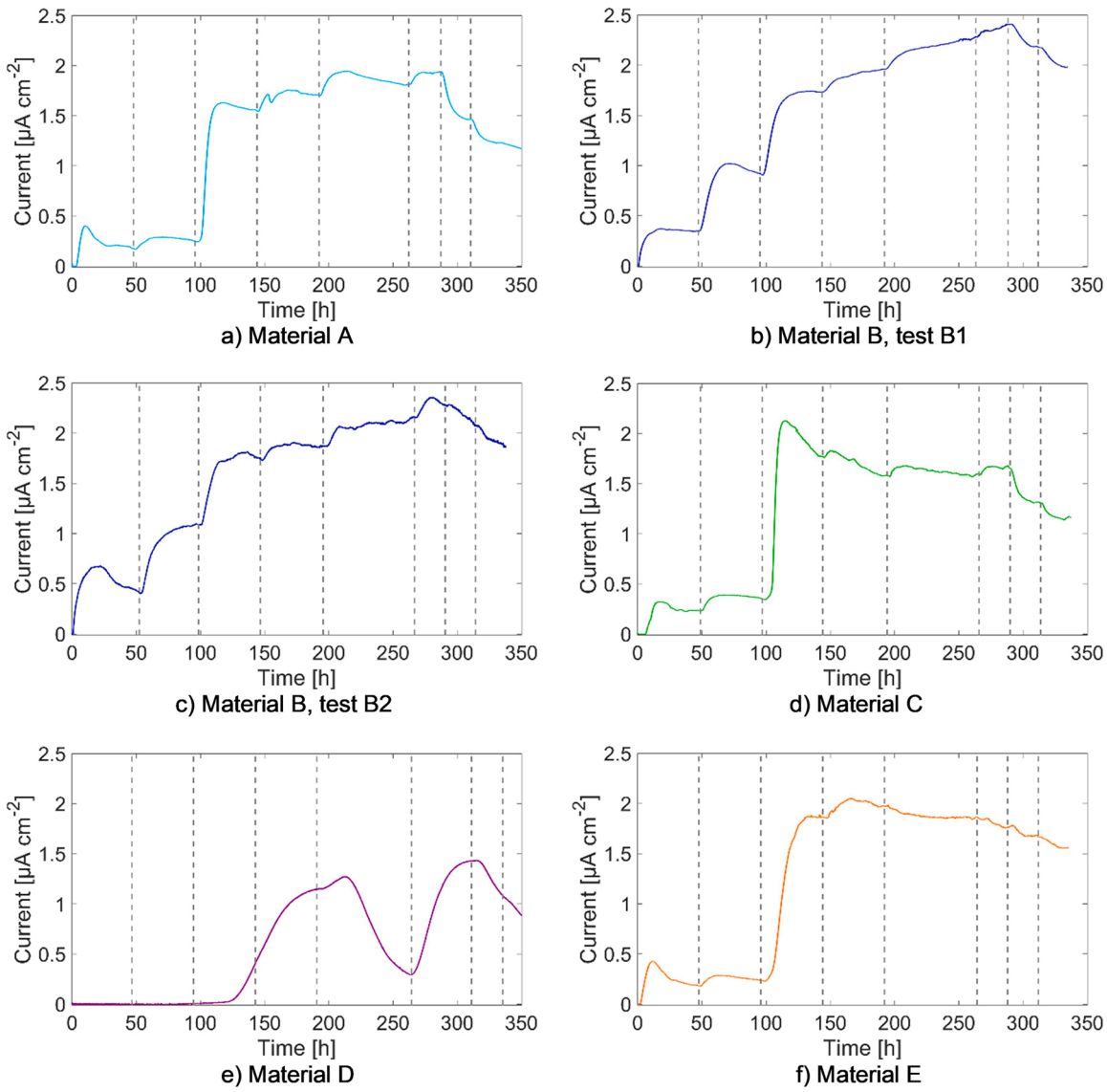

Fig. 8. Permeation current from the electrochemical hydrogen permeation tests. The dashed lines mark the steps with different p_{CO2} and p_{H2S}, as described in Table 3. The H_2S partial pressure was kept at 0.7 mbar H_2S about one day longer for Material D since the clogging of the gas supply to the corrosion compartment decreased the permeation current.

during CO_2 corrosion is strongly influenced by the corrosion mechanism. The corrosion rates and measured hydrogen uptakes increased when the CO_2 partial pressure was increased from 0.2 to 1 bar, but the permeation flux decreased after reaching a peak for all the transients observed in CO_2 environment, except the 1 bar CO_2 transient for Material B test 2 which reached a plateau. This indicates that the corroded surfaces created a barrier for hydrogen permeation under these conditions. The main change on the surfaces during CO_2 corrosion was the accumulation of retained carbides, which happened to a greater extent for the materials with low hydrogen uptakes, A, C and E, than for the material with the highest hydrogen uptake, Material B. Materials B and C have the lowest carbon contents, 0.28 and 0.35 wt% respectively, but very different hydrogen uptakes. There is a substantial difference in film weight between these materials, which cannot be explained by the difference in corrosion rate and carbon content but may be related to the carbide distribution in the metal. Material C has a microstructure with thin carbides on many of the ferrite grain boundaries, which may give a stronger adhesion between the corrosion products and steel, and thus more retained carbides and higher film weight. Overall, it appears that the presence of retained carbides reduced the hydrogen uptakes of the wire materials. The retained carbide is conductive and can therefore not limit the hydrogen uptake as a charge-transfer barrier, but possibly as a mass-transfer barrier. The increased corrosion rate of ferritic-pearlitic steels during selective dissolution of ferrite is explained by a larger active cathodic area, which means that the average distance between cathodic reaction sites and ferrite increases as well. Since cementite is considered an obstacle to hydrogen diffusion [39,40,47], the hydrogen that is adsorbed on cementite far from ferrite will have less opportunities for absorption and diffusion into the uncorroded steel compared to hydrogen adsorbed close to the ferrite. Possibly, it is only hydrogen that is reduced on ferrite or on carbides near ferrite that has a chance of being absorbed in the steel. If the retained carbide area is increasing faster than the corrosion rate, the cathodic current density will decrease, and less hydrogen will be reduced near ferrite. This is a possible mechanism for the presence of a peak hydrogen permeation flux during pure CO_2 corrosion. The proposed mechanism relies on a lower concentration of adsorbed hydrogen on and near the ferrite. The retained carbides are increasing the corrosion rate and hence the total amount of hydrogen reacting on the surface. If this effect dominates, the hydrogen uptake will increase with the amount of retained carbides rather than decrease,

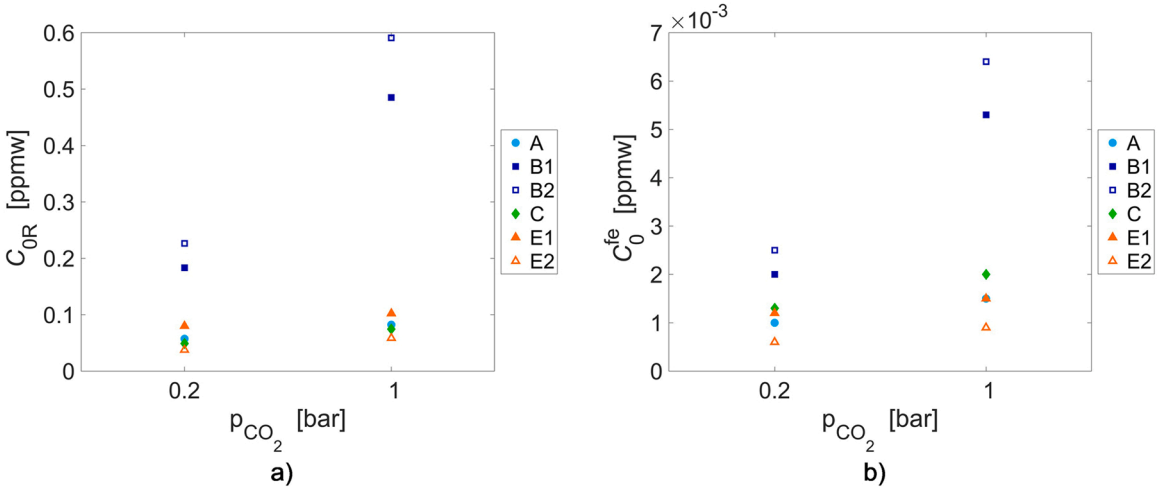

Fig. 9. Hydrogen uptakes estimated for the pure CO_2 period of the permeation tests, step 1 and 2 in Table 3. C_{0R} reflects both the lattice hydrogen and hydrogen in reversible traps whereas C_0^{fe} only describes the hydrogen in ferrite lattice.

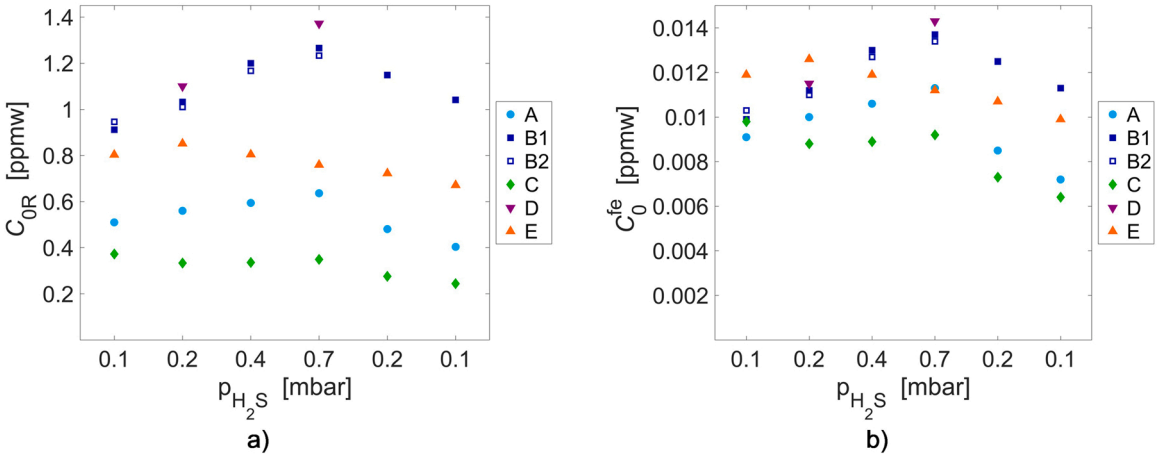

Fig. 10. Hydrogen uptakes estimated for the H_2S steps of the permeation test, step 3–8 in Table 3. C_{0R} reflects both the lattice hydrogen and hydrogen in reversible traps whereas C_0^{fe} only describes the hydrogen in lattice. The steps are placed in chronological order with the first exposure to H_2S placed to the left.

Table 7
Reversible hydrogen uptakes measured for uncorroded samples under cathodic polarization in previous work [31] and during step 6 of the permeation test (0.7 mbar H_2S).

Material	C_{0R} under cathodic polarization[a] [wt ppm]	C_{0R} during step 6[b] [wt ppm]
A	0.69	0.64
B	1.59	1.27
C	0.73	0.35
D	1.54	1.37
E	1.74	0.76

[a] 0.1 M NaOH, − 12 mA cm^{-2}, 25 °C.
[b] 0.7 mbar H_2S and 1 bar CO_2, 25 °C.

as observed by da Silva et al. [21].

4.3. Hydrogen uptake during H_2S exposure

H_2S is a hydrogen recombination poison [34,48,49] which can increase the hydrogen uptake in steels, while precipitation of FeS can both increase the hydrogen uptake by acting as a cathodic site [50] and decrease the hydrogen uptake by forming a barrier to hydrogen diffusion [25,26]. For all the materials, the hydrogen uptake decreased like a decay transient when the H_2S partial pressure was decreased in step 7 (0.2 mbar H_2S) and 8 (0.1 mbar H_2S), despite relatively stable corrosion rates, which indicates that the materials were subjected to a H_2S poison effect, even after the formation of S-containing corrosion products on the surfaces. The hydrogen recombination poison effect can also explain why the hydrogen uptakes increased when H_2S was added, despite decreased corrosion rates. A cathodic site effect may arise from the formation of mackinawite, which is expected to happen on the steel surface by reaction with the iron in metallic form [51], hence introducing new cathodic sites on the ferrite. This can give a shorter average path for hydrogen from adsorption site to ferrite matrix, compared to the path from retained carbides to ferrite matrix. However, cathodic reactions may still be occurring to a great extent on the retained carbides even during the H_2S exposure steps of the tests, especially if all the ferrite is covered with a thin FeS layer and the FeS layer has a high charge-transfer resistance. There are several indications of a barrier effect in the experiments: 1) Materials A, C and E had decreasing permeation fluxes after reaching a peak permeation flux in some of the H_2S exposure steps, 2) Materials C and E reached their highest hydrogen permeation flux before exposure to the highest H_2S partial pressure, and 3) Materials A, C, D and E had lower hydrogen permeation flux the second time the surfaces were exposed to 0.2 and 0.1 mbar H_2S compared to the first time, see Fig. 8. For Material A, C, D and E, there is

a relationship between film weight and C_{0R} during H_2S exposure. This relationship may be linked to the corrosion rate, where both the corrosion rate and film weight increases with the amount of retained carbides and the hydrogen uptake increases with the corrosion rate due to a higher amount of hydrogen being reduced at or near ferrite grains. It is also linked directly to the cementite, where the film weight increases with the amount of retained carbides on the surface and the hydrogen uptakes increase with the ferrite-cementite interfacial area due to trapping. Material B does however not follow this trend. Material B has the highest hydrogen uptake among the non-lamellar materials, both when considering only lattice hydrogen and hydrogen in reversible traps, despite having the lowest carbon content and film weight. If cathodic reactions are still occurring on the retained carbides, the same mechanism as proposed for CO_2 corrosion in Section 4.2 may be applicable for combined CO_2 and H_2S exposure. The behavior of materials A, C, D and E is consistent with the observations by Zhou et al. [27]. Under the condition of 1 MPa p_{CO2} and 0.001–0.1 MPa p_{H2S}, they found that the corrosion rate increased with the decrease of H_2S partial pressure and that the corrosion products changed from initially promoting hydrogen permeation to hindering the hydrogen permeation as the corrosion progressed. It is possible that this change from hydrogen promotion to hindrance would also be seen for Material B if the tests were conducted for longer times. Material B has a lower carbide fraction and corrosion rate than the other materials and might therefore need more time to form a well-covering FeS layer on the ferrite. This effect may be enhanced by lower adhesion between finely distributed carbides and steel surface, which keeps the ferrite fraction on the surface high through-out the CO_2 corrosion part of the test. Hence, more time may be needed for Material B to form the same barrier as the other materials, but this is questionable since the S content measured on the surfaces was not particularly low for Material B. There appears to be a trade-off between the positive and negative effects of retained carbides, where Material C has the best balance. Material B appears to have too little carbide, or too poorly connected carbide, to receive the beneficial effect of retained carbides. The materials with higher carbide contents than Material C also have higher hydrogen uptakes due to hydrogen trapping on carbide-cementite interfaces, possibly with contribution from higher corrosion rates.

5. Conclusion

Five steel armor wires were exposed to artificial seawater bubbled with N_2, CO_2 and H_2S in an electrochemical hydrogen permeation cell while the hydrogen permeation flux through the steels was measured. The electrolyte was continuously replaced to simulate an environment where protective iron carbonate film formation is not thermodynamically favorable.

- The hydrogen uptakes decreased with the accumulation of retained carbide for most of the materials, despite increasing corrosion rates. The carbide is primarily a site for cathodic reactions and the proposed mechanism for the reduced hydrogen uptakes with retained carbides is that the hydrogen adsorbed on retained carbides located far from ferrite grains will have limited opportunities for absorption into the steel since the hydrogen solubility and diffusivity in cementite is low.
- The positive effect of retained carbides was observed during pure CO_2 corrosion and when small amounts of H_2S (< 1 mbar H_2S) was introduced to the environment.
- The material with the lowest and most stable corrosion rate during CO_2 corrosion was one of the materials with highest hydrogen uptake. This material has the lowest carbon content and less continuous carbides than the other materials, and hence less retained carbides.
- Apart from this material, the results indicated higher hydrogen uptake with higher carbon content, probably due to the trapping of hydrogen on ferrite-cementite interfaces.
- Despite the reduction of hydrogen uptake with time observed for most of the materials, the hydrogen uptakes decreased substantially when the H_2S partial pressure was reduced towards the end of the tests, indicating a strong sensitivity to the H_2S poison effect even after the formation of hydrogen uptake barrier.

CRediT authorship contribution statement

Ellen Synnøve Skilbred: Conceptualization, Methodology, Investigation, Resources, Data curation, Writing – original draft, Visualization. **Simona Palencsár:** Conceptualization, Methodology, Validation, Investigation, Data curation, Writing – review & editing, Project administration. **Arne Dugstad:** Conceptualization, Methodology, Writing – review & editing, Supervision, Funding acquisition. **Roy Johnsen:** Conceptualization, Methodology, Writing – review & editing, Supervision, Funding acquisition.

Declaration of Competing Interest

The authors declare that they have no known competing financial interests or personal relationships that could have appeared to influence the work reported in this paper.

Data availability statement

The raw/processed data generated in this work are available upon request from the corresponding author.

Acknowledgements

This work was performed as part of the KPN project "Environmental Cracking of Flexible Pipe Armour Wires", Research Council of Norway project no. 280760 within the PETROMAKS 2 program. The authors would like to thank the following project participants for financial and technical support: The Research Council of Norway, Norway; Equinor, Norway; Shell, Norway; Chevron, United States of America; Petrobras, Brazil; OKEA, Norway; TechnipFMC, France; NOV, Denmark; Baker Hughes, United Kingdom; 4Subsea, Norway.

References

[1] T. Campos, J.A. Gomes, M. Seiersten, S. Palencsár, A. Dugstad, Corrosion of Armor Wire Steel in the Annulus of Flexible Pipes at Near Neutral pH, in: Corros. 2019, NACE International, Nashville, TN, 2019.
[2] A. Rubin, M.H. Haarh, S. Overby, T.S. Nielsen, J. Gudme, Corrosion Rates of Carbon Steel in Confined Environments. Corros. 2012, NACE International,, Salt Lake City, Utah, 2012, pp. 4002–4019.
[3] E. Remita, F. Ropital, J. Kittel, B. Tribollet, E. Sutter, C. Taravel-Condat, N. Desamais, Experimental and theoretical investigatoin of the uniform corrosion in the annulus of offshore flexible pipelines, in: Corros. 2008, New Orleans, Louisiana, 2008, pp. 4737–4753.
[4] W. Sun, S. Nešić, Kinetics of corrosion layer formation: part 1—iron carbonate layers in carbon dioxide corrosion, Corrosion 64 (2008) 334–346, https://doi.org/10.5006/1.3278477.
[5] S. Nešić, Key issues related to modelling of internal corrosion of oil and gas pipelines – A review, Corros. Sci. 49 (2007) 4308–4338, https://doi.org/10.1016/j.corsci.2007.06.006.
[6] S. Nesic, A. Stangeland, R. Nyborg, M. Nordsveen, A. Mechanistic Model for CO2 Corrosion with Protective Iron Carbonate Films, in: Corros. 2001, Houston, TX, 2001.
[7] L.L. Shreir, R.A. Cottis, Corrosion in liquids, corrosion evaluation, in: B. Cottis, M. Graham, R. Lindsay, S. Lyon, T. Richardson, D. Scantlebury, H. Scott (Eds.), Shreir's Corros, 4th ed..,, Elsevier, Amsterdam, 2010, pp. 725–1692.
[8] D. Burkle, R. De Motte, W. Taleb, A. Kleppe, T. Comyn, S.M. Vargas, A. Neville, R. Barker, In situ SR-XRD study of FeCO3 precipitation kinetics onto carbon steel in CO_2-containing environments: the influence of brine pH, Electrochim. Acta 255 (2017) 127–144, https://doi.org/10.1016/j.electacta.2017.09.138.
[9] D.A. López, W.H. Schreiner, S.R. de Sánchez, S.N. Simison, The influence of carbon steel microstructure on corrosion layers: an XPS and SEM characterization, Appl. Surf. Sci. 207 (2003) 69–85, https://doi.org/10.1016/S0169-4332(02)01218-7.
[10] C.A. Zapffe, C.E. Sims, Hydrogen Embrittlement, in: Internal Stress and Defects in Steel, Trans, 145, AIME, 1941, pp. 225–261.

[11] D.G. Westlake, A generalized model for hydrogen embrittlement, Trans. ASM 62 (1969) 1000–1006.

[12] M. Hatano, M. Fujinami, K. Arai, H. Fujii, M. Nagumo, Hydrogen embrittlement of austenitic stainless steels revealed by deformation microstructures and strain-induced creation of vacancies, Acta Mater. 67 (2014) 342–353, https://doi.org/10.1016/j.actamat.2013.12.039.

[13] C.D. Beachem, A new model for hydrogen-assisted cracking (hydrogen "embrittlement"), Metall. Mater. Trans. B 3 (1972) 441–455, https://doi.org/10.1007/BF02642048.

[14] H.K. Birnbaum, P. Sofronis, Hydrogen-enhanced localized plasticity—a mechanism for hydrogen-related fracture, Mater. Sci. Eng. A. 176 (1994) 191–202, https://doi.org/10.1016/0921-5093(94)90975-X.

[15] A.R. Troiano, The role of hydrogen and other interstitials in the mechanical behavior of metals (1959 Edward De Mille Campbell Memorial Lecture), Trans. Am. Soc. Met. 52 (1960) 54–80.

[16] R. Kirchheim, Revisiting hydrogen embrittlement models and hydrogen-induced homogeneous nucleation of dislocations, Scr. Mater. 62 (2010) 67–70, https://doi.org/10.1016/j.scriptamat.2009.09.037.

[17] P. Kedzierzawski, Hydrogen Trapping in Iron and Iron Alloys, in: R.A. Oriani, J. P. Hirth, M. Smialowski (Eds.), Hydrog. Degrad. Ferr. Alloy., 4th ed..,, William Andrew Publishing/Noyes, 1985, pp. 271–288.

[18] T.P. Radhakrishnan, L.L. Shreir, Permeation of hydrogen through steel by electrochemical transfer - I. Influence of catalytic poisons, Electrochim. Acta 11 (1966) 1007–1021.

[19] F. Farelas, M. Galicia, B. Brown, S. Nesic, H. Castaneda, Evolution of dissolution processes at the interface of carbon steel corroding in a CO_2 environment studied by EIS, Corros. Sci. 52 (2010) 509–517, https://doi.org/10.1016/j.corsci.2009.10.007.

[20] A. Dugstad, Mechanism of Protective Film Formation During CO_2 Corrosion of Carbon Steel, in: Corros. 1998, NACE International, 1998.

[21] S.C. da Silva, E.A. de Souza, F. Pessu, Y. Hua, R. Barker, A. Neville, J.A. da Cunha Ponciano Gomes, Cracking mechanism in API 5L X65 steel in a CO_2-saturated environment, Eng. Fail. Anal. 99 (2019) 273–291, https://doi.org/10.1016/j.engfailanal.2019.02.031.

[22] D.N. Staicopolus, The role of cementite in the acidic corrosion of steel, J. Electrochem. Soc. 110 (1963) 1121, https://doi.org/10.1149/1.2425602.

[23] J.L. Crolet, N. Thevenot, S. Nesic, Role of conductive corrosion products in the protectiveness of corrosion layers, Corrosion 54 (1998).

[24] C. Plennevaux, J. Kittel, M. Frégonèse, B. Normand, F. Ropital, F. Grosjean, T. Cassagne, Contribution of CO_2 on hydrogen evolution and hydrogen permeation in low alloy steels exposed to H2S environment, Electrochem. Commun. 26 (2013) 17–20, https://doi.org/10.1016/j.elecom.2012.10.010.

[25] E. Wallaert, T. Depover, I. De Graeve, K. Verbeken, FeS corrosion products formation and hydrogen uptake in a sour environment for quenched & tempered steel, Met 8 (2018), https://doi.org/10.3390/met8010062.

[26] F. Huang, P. Cheng, X.Y. Zhao, J. Liu, Q. Hu, Y.F. Cheng, Effect of sulfide films formed on X65 steel surface on hydrogen permeation in H2S environments, Int. J. Hydrog. Energy 42 (2017) 4561–4570, https://doi.org/10.1016/j.ijhydene.2016.10.130.

[27] C. Zhou, B. Fang, J. Wang, S. Hu, B. Ye, Y. He, J. Zheng, L. Zhang, Effect of interaction between corrosion film and $H2S/CO_2$ partial pressure ratio on the hydrogen permeation in X80 pipeline steel, Corros. Eng. Sci. Technol. 55 (2020) 392–399, https://doi.org/10.1080/1478422X.2020.1737384.

[28] A. Dugstad, S. Palencsár, G. Svenningsen, J. Muren, M. Eriksen, B. Thoppil, J. Melville, K. Sanghavi, The Combined Effect of O2 and CO2 on Corrosion of Flexible Armour Wires, in: Corros. 2020, 2020: p. NACE-2020–14790.

[29] A. Dugstad, S. Palencsár, T. Berntsen, L. Børvik, Corrosion of steel armour wires in flexible pipes - history effects (Aberdeen, Scotland, UK), SPE Int. Oilf. Corros. Conf. Exhib. (2018) 1–16, https://doi.org/10.2118/190907-MS.

[30] M.A.V. Devanathan, Z. Stachurski, The adsorption and diffusion of electrolytic hydrogen in palladium, Proc. R. Soc. Lond. A. Math. Phys. Sci. 270 (1962) 90–102. ⟨http://www.jstor.org/stable/2416199⟩.

[31] E.S. Skilbred, M. Kappes, M. Iannuzzi, R. Johnsen, Hydrogen uptake and diffusivity in steel armor wires with different chemical composition, carbide distribution, grain size, and degree of deformation, Mater. Corros. (2021) 1–20, https://doi.org/10.1002/maco.202112615.

[32] American Petroleum Institute, API Specification 17J: Specification for Unbonded Flexible Pipe, 4th edition, 2014.

[33] NACE Standard TM0198 Slow Strain Rate Test Method for Screening Corrosion-Resistant Alloys for Stress Corrosion Cracking in Sour Oilfield Service, (2016).

[34] ASTM G148 Standard Practice for Evaluation of Hydrogen Uptake, Permeation, and Transport in Metals by an Electrochemical Technique, (2018).

[35] ISO 17081. Method of measurement of hydrogen permeation and determination of hydrogen uptake and transport in metals by an electrochemical technique, (2014).

[36] P. Bruzzoni, Efectos de superficie en la difusión de hidrógeno en hierro y aleaciones ferrosas, Universidad de Buenos Aires, 2003.

[37] H. Husby, M. Iannuzzi, R. Johnsen, M. Kappes, A. Barnoush, Effect of nickel on hydrogen permeation in ferritic/pearlitic low alloy steels, Int. J. Hydrog. Energy 43 (2018) 3845–3861, https://doi.org/10.1016/j.ijhydene.2017.12.174.

[38] D. Johnson, G. Krauss, Correlation of microstructural parameters and hydrogen permeation in carbon steel, Metall. Trans. A. 18 A (1987) 717–721.

[39] W.C. Luu, J.K. Wu, The influence of microstructure on hydrogen transport in carbon steels, Corros. Sci. 38 (1996) 239–245, https://doi.org/10.1016/0010-938X(96)00109-6.

[40] G.M. Pressouyre, Hydrogen traps, repellers, and obstacles in steel; Consequences on hydrogen diffusion, solubility, and embrittlement, Metall. Trans. A. 14 (1983) 2189–2193, https://doi.org/10.1007/BF02662391.

[41] K. Kiuchi, R.B. McLellan, The solubility and diffusivity of hydrogen in well-annealed and deformed iron, Acta Met. 31 (1983) 961–984, https://doi.org/10.1016/0001-6160(83)90192-X.

[42] C. Forot, E. Legrand, E. Roguet, J. Creus, J. Kittel, X. Feaugas, Impact of cementite tortuosity on hydrogen diffusion in pearlitic steels, in: Eurocorr 2015, Graz, Austria, 2015, pp. 107–114. ⟨https://hal-ifp.archives-ouvertes.fr/hal-02464473⟩.

[43] A. Turnbull, R.B. Hutchings, Analysis of hydrogen atom transport in a two-phase alloy, Mater. Sci. Eng. A. 177 (1994) 161–171, https://doi.org/10.1016/0921-5093(94)90488-X.

[44] F. Thebault, S. Frappart, L. Delattre, H. Marchebois, J. Creus, X. Feaugas, Hydrogen Diffusion In a Model Molybdenum Containing Steel: A Comparison Between Hydrogen Ingress Promoted By H2S Or Cathodic Charging, in: Corros. 2011, NACE International, Houston, Texas, 2011, p. 11104 (NACE).

[45] D. Rickard, G.W. Luther, Chemistry of iron sulfides, Chem. Rev. 107 (2007) 514–562, https://doi.org/10.1021/cr0503658.

[46] K.-L. Lee, S. Nesic, The Effect of Trace Amount of H2S on CO_2 Corrosion Investigated by Using the EIS Technique, in: Corros. 2005, 2005, p. 05630 (NACE).

[47] L. Tau, S.L.I. Chan, Effects of ferrite/pearlite alignment on the hydrogen permeation in a AISI 4130 steel, Mater. Lett. 29 (1996) 143–147, https://doi.org/10.1016/S0167-577X(96)00140-1.

[48] K.A. Esaklul, 13 - Hydrogen damage, in: A.M.B.T.-T. in O. and G.C. R. and T. El-Sherik (Ed.). Woodhead Publ. Ser. Energy, Woodhead Publishing,, Boston, 2017, pp. 315–340, https://doi.org/10.1016/B978-0-08-101105-8.00013-9.

[49] X. Wen, P. Bai, B. Luo, S. Zheng, C. Chen, Review of recent progress in the study of corrosion products of steels in a hydrogen sulphide environment, Corros. Sci. 139 (2018) 124–140, https://doi.org/10.1016/j.corsci.2018.05.002.

[50] P. Bai, Y. Liang, S. Zheng, C. Chen, Effect of amorphous FeS semiconductor on the corrosion behavior of pipe steel in H2S-containing environments, Ind. Eng. Chem. Res. 55 (2016) 10932–10940, https://doi.org/10.1021/acs.iecr.6b03000.

[51] W. Sun, S. Nesic, A. Mechanistic, Model Of H2S corrosion of mild steel, Corros. 2007, Athens, Ohio (2007) 07655 (Paper No.).